Article type:

(Full paper)

Reduced Bilateral Recombination by Functional Molecular Interface Engineering for Efficient Inverted Perovskite Solar Cells

Bowei Li[a,1], Yuren Xiang[a,1], K. D. G. Imalka Jayawardena[a], Deying Luo[c], Zhuo Wang[d], Xiaoyu Yang[f], John F. Watts[e], Steven Hinder[e], Muhammad T. Sajjad[g], Thomas Webb[a], Haitian Luo[h], Igor Marko[b], Hui Li[a,h], Stuart A. J. Thomson[i], Rui Zhu[f], Guosheng Shao[d], Stephen J. Sweeney[b], S. Ravi P. Silva[a,*], Wei Zhang[a,*]

[a] Advanced Technology Institute, Department of Electrical and Electronic Engineering, University of Surrey, Guildford, Surrey, GU2 7XH, UK

[b] Advanced Technology Institute and Department of Physics, University of Surrey, Guildford, Surrey, GU2 7XH, UK

[c] Department of Materials Science and Engineering, University of Toronto, Toronto M5G 3E4, Canada

[d] State Center for International Cooperation on Designer Low-carbon & Environmental Materials (CDLCEM), Zhengzhou University, 100 Kexue Avenue, Zhengzhou 450001, China

[e] The Surface Analysis Laboratory, Department of Mechanical Engineering Sciences, University of Surrey, Guildford, Surrey, GU2 7XH, UK

[f] State Key Laboratory for Artificial Microstructure and Mesoscopic Physics, School of Physics, Frontiers Science Center for Nano-optoelectronics & Collaborative Innovation Center of Quantum Matter, Peking University, Beijing 100871, China

[g] Centre for Energy Engineering, School of Engineering, London South Bank University,103 Borough Road, London, SE1 0AA, UK

[h] Institute of Electrical Engineering, Chinese Academy of Sciences, Beijing 100190, China

[i] Edinburgh Instruments Ltd., 2 Bain Square, Livingston, EH54 7DQ, UK

*Corresponding author. E-mail: wz0003@surrey.ac.uk; s.silva@surrey.ac.uk

[1]These authors contributed equally.

Abstract

Interface-mediated recombination losses between perovskite and charge transport layers are one of the main reasons that limit the device performance, in particular for the open-circuit voltage (V_{OC}) of perovskite solar cells (PSCs). Here, functional molecular interface engineering (FMIE) is employed to retard the interfacial recombination losses. The FMIE is a facile solution-processed means that introducing functional molecules, the fluorene-based conjugated polyelectrolyte (CPE) and organic halide salt (OHS) on both contacts of the perovskite absorber layer. Through the FMIE, the champion PSCs with an inverted planar heterojunction structure show a remarkable high V_{OC} of 1.18 V whilst maintaining a fill factor (FF) of 0.83, both of which result in improved power conversion efficiencies (PCEs) of 21.33% (with stabilized PCEs of 21.01%). In addition to achieving one of the highest PCEs in the inverted PSCs, the results also highlight the synergistic effect of these two molecules in improving device performance. Therefore, the study provides a straightforward avenue to fabricate highly efficient inverted PSCs.

1 Introduction

Inverted perovskite solar cells (PSCs), by sandwiching a perovskite absorber between a p-type and n-type charge transport layer, have been at the forefront of perovskite photovoltaics because of the simplified device configuration, easy fabrication and improved operational stability [1–8]. The inverted PSCs are compatible with scalable solution deposition methods, such as doctor-blade coating [9] and slot-die coating with the roll-to-roll process [10], which enable industrial manufacture of large-area devices. Besides, this type of device offers the promise approaching the thermodynamic limit when incorporated into tandem cells [11–15]. All these advantages of inverted PSCs have attracted growing research interests and significant efforts have been dedicated to further improving the device efficiency and operational stability, including compositional tuning [14,16], interface engineering [4–6,17,18], and materials design of charge transport layers [19,20].

In the inverted PSCs, the p-type layers close to the transparent electrodes are regarded as the hole transporting layers (HTLs), which play an important role in governing the hole transport and perovskite crystallization. Generally, HTLs are divided into two categories: inorganic (e.g. metal oxides or compounds) and organic (e.g. small molecules or polymers) materials. The inorganic HTLs are commonly presenting surface traps [21] or inferior mechanical flexibility [20,22], leading to fewer applications on plastic substrates. Therefore, organic HTLs are superior alternatives thanks to readily tunable properties, low-temperature processing and commercial availability [4–7], maintaining the highest efficiency (certified 22.3%) in inverted PSCs [23]. Amongst organic HTLs, poly(N,N′-bis(4-butylphenyl)-N,N′-bis(phenyl)benzidine) (poly-TPD) has proven to be a representative material, with favorable energy levels, high intrinsic hole mobility and thermal stability [24–29]. Inverted PSCs using poly-TPD HTLs also exhibit excellent indoor performance [30]. Encouragingly, poly-TPD based two-terminal (2T) perovskite-on-silicon tandem solar cells surpass the record efficiency

3

of monocrystalline solar cells [14], showing the bright future for practical applications. However, despite these substantial improvements, it is still challenging to further improve device performance of single-junction inverted PSCs with poly-TPD HTLs owing to serious interfacial recombination losses [14,31,32]. These losses not only exist at the poly-TPD/perovskite interface but also are prone to generate at perovskite/electron transport layer (ETL) interface when using fullerene derivatives as the ETLs [6,31,33]. Hence, more attention should be paid to the interfaces adjacent to the perovskite absorbers.

In this study, we reported a functional molecular interface engineering (FMIE) approach to simultaneously improve both interfaces (namely, the HTL/perovskite interface and perovskite/ETL interface). Specifically, we spin-coated the fluorene-based conjugated polyelectrolyte (CPE) on top of poly-TPD and organic halide salt (OHS) on top of perovskite layer, respectively. It is found that the introduction of the CPE has a positive impact on reducing interfacial recombination thanks to the efficient charge transfer, as evidenced by the steady-state photoluminescence (PL), time-resolved photoluminescence (TRPL) decay, space-charge limited current (SCLC) and electrical impedance spectroscopy (EIS) measurements. In-depth light-intensity-dependent photo-response analysis and theoretical calculations further confirm that the OHS could mitigate the interfacial recombination at the perovskite/ETL interface as a result of passivating surface defects. The tailored PSCs with an inverted planar architecture show a champion PCE of 21.33%, with a significant enhancement in both the open-circuit voltage (V_{OC}) and fill factor (FF) compared to the control devices without FMIE.

2 Experimental Section

2.1 Materials

Poly-TPD (M_w is ~85 k) and PFN-Br were purchased from 1-Material. F4TCNQ was purchased from Xi'an Polymer Light Technology Corp. (China). Lead diiodide (PbI$_2$, 99.99%) and lead

4

dibromide (PbBr$_2$, 99%) were purchased from Tokyo Chemical Industry Co., Ltd. (TCI, Japan). Formamidinium iodide (FAI), methylammonium iodide (MAI), phenylammonium iodide (PAI), phenylmethylamine iodide (PMAI, also called benzylammonium iodide) and phenethylammonium iodide (PEAI) were purchased from Greatcell Solar Materials Pty Ltd. Cesium iodide (CsI, 99.999%) was purchased from Sigma-Aldrich. PC$_{61}$BM (99.5%) was purchased from Solenne. Bathocuproin (BCP, 98%) was purchased from Alfa Aesar. N,N-dimethylformamide (DMF, 99.8%), dimethyl sulfoxide (DMSO, 99.7%), chlorobenzene (CB, 99.8%) and toluene (99.85%) were purchased from Acros and the other solvents were purchased from Sigma-Aldrich. All chemicals were purchased from commercial suppliers and used as received.

2.2 Device fabrication

The detailed fabrication process can be found in our previous report [32]. Briefly, pre-patterned ITO glass (20 × 20 mm^2) was cleaned by ultrasonication with detergent, deionized water, acetone and isopropanol (IPA). The poly-TPD solution (1 mg mL^{-1} in toluene with 0.2 mg mL^{-1} F4TCNQ) was spin-coated on cleaned ITO (10 min O$_2$ plasma Asher) at a speed of 2000 rpm (2000 rpm s^{-1}) for 30 s and then annealed at 130 °C for 10 min. Before depositing perovskite film, the poly-TPD film was modified by spin coating 0.4 mg mL^{-1} PFN-Br at 5000 rpm (2500 rpm s^{-1}) for 30 s or treated by 20s UV-ozone. For perovskite film deposition, the stoichiometric precursor Cs$_{0.05}$FA$_{0.79}$MA$_{0.16}$PbI$_{2.4}$Br$_{0.6}$ made by dissolving PbI$_2$, PbBr$_2$, FAI, MAI, CsI in 1 mL DMF:DMSO (4:1 V/V) was spin-coated on the modified poly-TPD by a two-consecutive step program at 1000 rpm for 10 s and 6000 rpm for 35 s. During the second step, the films were quickly washed by 100 μL of CB at 5 s before the end of the program. Subsequently, the samples were annealed on a hotplate at 90 °C for 80 min. For the passivation layer, PAI, PMAI, PEAI solution (0.5 to 4 mg dissolved in 1 mL IPA) was spin-coated on perovskite surface at 5000 rpm (2500 rpm s^{-1}) for 30 s when the samples were fully cooled down. Then, PC$_{61}$BM solution (30 mg mL^{-1} in CB) and BCP solution (0.5 mg mL^{-1} in IPA) were spin-coated with the program

of 2500 rpm (30 s) and 5000 rpm (25 s) in order. The devices were finished by thermally evaporated silver (100 nm).

2.3 Characterization

The surface morphologies were studied by SEM (Jeol 7100F) and AFM (Bruker ICON2 SYS). 100 grains in each SEM image were analyzed by Image J software to obtain the grain size distribution. XRD patterns were performed by PANalytical X'Pert Pro. ToF-SIMS analyses were carried out on an ION-TOF GmbH (Münster, Germany) TOF.SIMS 5 system. PL and TRPL were performed in an FLS1000 Photoluminescence Spectrometer. The absorption spectra were performed by Varian Cary 5000 UV-vis-NIR spectrophotometer. The film thickness was measured by a surface profilometer (Dektak XT). The J-V characteristics were performed outside the glovebox using a Keysight 2400 Source Meter under simulated one-sun AM 1.5G illumination (100 mW cm^{-2}) with a solar simulator (Enlitech, SS-F5-3A) calibrated by using a standard monocrystalline silicon solar cell with a KG-5 filter [5]. All devices were measured both in the reverse scan $(1.2 \rightarrow -0.2 \text{ V}, \text{step } 0.02 \text{ V})$ and forward scan $(-0.2 \rightarrow 1.2 \text{ V}, \text{step } 0.02 \text{ V})$. To ensure accuracy, a mask with an aperture area of 0.09 cm^2 was employed during the measuring process. The stabilized power output was measured under the largest power output bias voltage. EQE was measured in air on a commercial system (Bentham PV300). For EL measurements, a Keithley 2420 Source Meter was used to apply a DC bias. Light out was measured using an Ocean Optics STS-NIR fiber-coupled spectrometer. For the LED external quantum efficiency measurements (LED-EQE), the electroluminescence was measured directly using a calibrated silicon photodetector (Newport 918D-SL-OD3R). For TPV measurements, a continuous wave white light bias was generated under illumination close to 0.1 Sun. A green LED was used as the perturbation source with a pulse width of 3 μs and a repetition frequency of 30 Hz. The LED rise and decay time constant were measured to be ~100 ns, therefore light pulses of the were nearly repeating electrical pulses from an Agilent 8114A pulse generator used in the experiments and had a square shape with ~100 ns rise and

decay time constant. The voltage under open circuit condition was measured using 1 MΩ input impedance and was recorded using a Tektronix MDO3014 1 GHz digital oscilloscope. EIS was conducted by using the Keysight B1500A system in a frequency range of 1 KHz~1 MHz applied at V_{OC} bias under the dark condition. The DFT calculations were performed by the referred computational methods [23,34,35].

3 Results and discussion

We first attempted two approaches to improve the surface wettability of the poly-TPD, by UV-ozone [27] or poly[(9,9-bis(3'-(N,N-dimethyl)-N-ethylammonium)-propyl)-2,7-flu-orene)-*alt*-2,7-(9,9-di-octylfluor-ene)] dibromide (PFN-Br) treatment [29], which is commonly encountered when organic HTLs are employed due to their hydrophobic nature. After treatments, the PFN-Br treated poly-TPD film shows a slightly smoother surface than that of UV-ozone treated (**Figure S1**), which may be beneficial for the following contact with the perovskite film. To further illustrate this impact, we performed topographic studies on perovskite films. As shown in **Figure 1a**, the scanning electron microscopy (SEM) and atomic force microscopy (AFM) demonstrate that there is no obvious difference in morphologies between the perovskite films. X-ray diffraction (XRD) also shows negligible new phases in perovskite films**,** except a promoted grain orientation along the [100] direction for PFN-Br treated sample (**Figure S2**), which indicates that the underlying PFN-Br layer could improve the crystallinity of the upper perovskite film [23,36]. Interestingly, by comparing **Figure 1b** and **Figure 1c**, the ion distributions in the cross-sectional perovskite films determined by time-of-flight secondary ion mass spectrometry (ToF-SIMS) clearly show that the PFN-Br has diffused into the perovskite film and accumulated near the surface, consistent with literature reported previously [32,37].
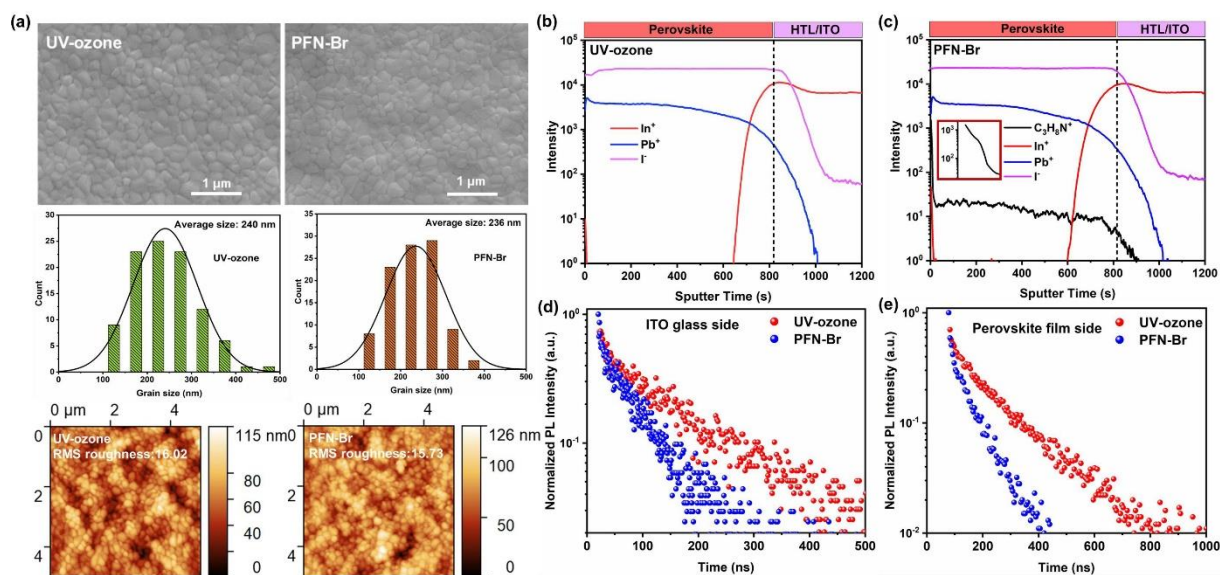
Figure 1. Properties of perovskite films deposited on the ITO glass/poly-TPD with UV-ozone or PFN-Br treatment. a) Morphologies of perovskite absorbers, including top-view SEM images, grain size distributions and the root-mean-square (RMS) roughnesses obtained from AFM images. b) ToF-SIMS depth profile of UV-ozone treated sample. c) ToF-SIMS depth profile of PFN-Br treated sample. Note that the $C_3H_8N^+$ is attributed to PFN-Br and the inset is the magnification of PFN-Br intensity near the perovskite surface. d) TRPL spectra excited from the ITO glass side. e) TRPL spectra excited from the perovskite film side.

Since the diffused PFN-Br might influence the carrier dynamics of perovskite films, we conducted the steady-state PL and TRPL measurements. When excited from the ITO glass side, the PFN-Br treated sample shows a significant steady-state PL quench (**Figure S3a**) and a reduced lifetime compared to UV-ozone treated sample (**Figure 1d, Table S1**), indicating a more efficient hole-extraction at the poly-TPD/perovskite interface. When excited from the perovskite film side, the steady-state PL (**Figure S3b**) and TRPL spectra (**Figure 1e**) display a similar trend, which could be attributed the charge extraction property of the PFN-Br thin layer [38] as the PFN-Br is predominately accumulated near the perovskite surface (see inset of **Figure 1c**). Therefore, introducing a functional polymer PFN-Br leads to faster charge-carrier transport compared to the physical UV-ozone treatment. This efficient extraction means the possibility of charge-carrier recombination could be reduced [22] and potentially will benefit the performance of the derived solar cells. To confirm our hypothesis, we fabricated the inverted

PSCs with the structure of ITO glass/poly-TPD/perovskite/[6,6]-phenyl-C61-butyric acid methyl ester (PCBM)/bathocuproine (BCP)/Ag, where the poly-TPD was treated by UV-ozone or PFN-Br, respectively. The current density-voltage (J-V) characteristics of the champion devices are shown in **Figure S4a**. Compared to the UV-ozone treatment, the PFN-Br treated devices show an increase in the PCEs from 18.75 to 20.07%, mainly driven by the improved short-circuit current density (J_{SC}) from 21.34 to 22.21 mA cm^{-2}. These J_{SC} values were further confirmed by the external quantum efficiency (EQE) measurements. **Figure S4b** shows improved photocurrents of PFN-Br treated devices in the visible light region (from 380 to 740 nm), consistent with the enhanced quality of perovskite films and charge-carrier extraction at the contact interface as shown in **Figure 1**.

For an in-depth understanding of charge dynamics, we first conducted SCLC measurement. The dark J-V curves of hole-only devices were measured with a structure of ITO glass/poly-TPD/UV-ozone or PFN-Br/perovskite/Spiro-OMeTAD/Ag. The traps density (N_t) is calculated by the following equation with trap-filled limit voltage (V_{TFL}, in **Figure S5a**):

$$N_t = \frac{2\varepsilon_o \varepsilon V_{TFL}}{e \mathrm{L}^2} \qquad\qquad ` \qquad (1)$$

Where ε_o, ε, e, L are the vacuum permittivity, the relative dielectric constant (46.9 for triple-cation perovskite) [39], elementary charge, perovskite thickness, respectively. The PFN-Br sample shows a lower N_t (3.35×10^{15} cm^{-3}) than that of UV-ozone treated sample (14.69×10^{15} cm^{-3}), which indicates an interfacial recombination suppression induced by PFN-Br. Furthermore, the EIS of devices processed by the UV-ozone and PFN-Br treatment is measured at V_{OC} bias under dark conditions [40]. As shown in **Figure S5b**, the PFN-Br treated device presents a smaller semicircle than that of UV-ozone in the Nyquist plots. Since the high-frequency component is related to the charge transfer, the plots were then fitted by using an equivalent circuit model (see inset of **Figure S5b**), including a total series resistance (R_s), a charge transfer resistance (R_{tr}) and a capacitance (C_{tr}). In contrast to the slight difference in R_s

and C_{tr}, the R_{tr} of PFN-Br treated device (R_{tr} = 17.95 Ω) is three times smaller than that of the U-ozone treated device (R_{tr} = 65.25 Ω) (**Table S2**). This indicates a more efficient charge extraction caused by the PFN-Br interfacial modification [41,42].

As a comparison, we also tried to add PFN-Br in the perovskite precursor solution directly, but the perovskite film still cannot fully cover the substrate without PFN-Br pre-treatment (**Figure S6**). This indicates that adding PFN-Br in the perovskite precursor solution cannot replace the function of the interfacial modification by PFN-Br, even though it seems to be a more straightforward approach by reducing an extra spin-coating step. Furthermore, the microscopic details in SEM images (**Figure S7a**) show that the amount of PFN-Br could influence the surface morphologies of the perovskite films. With the increase of PFN-Br concentration, the topography of the perovskite film becomes coarser, leading to device efficiency degradation (**Figure S7b**). We suspect that the additional PFN-Br might disturb the perovskite crystallization and act as recombination centers in perovskite [4]. Besides, it is more challenging to control the distribution of PFN-Br in the perovskite film through this method. Therefore, these results further confirm the necessity of the PFN-Br modification at the poly-TPD/perovskite interface.
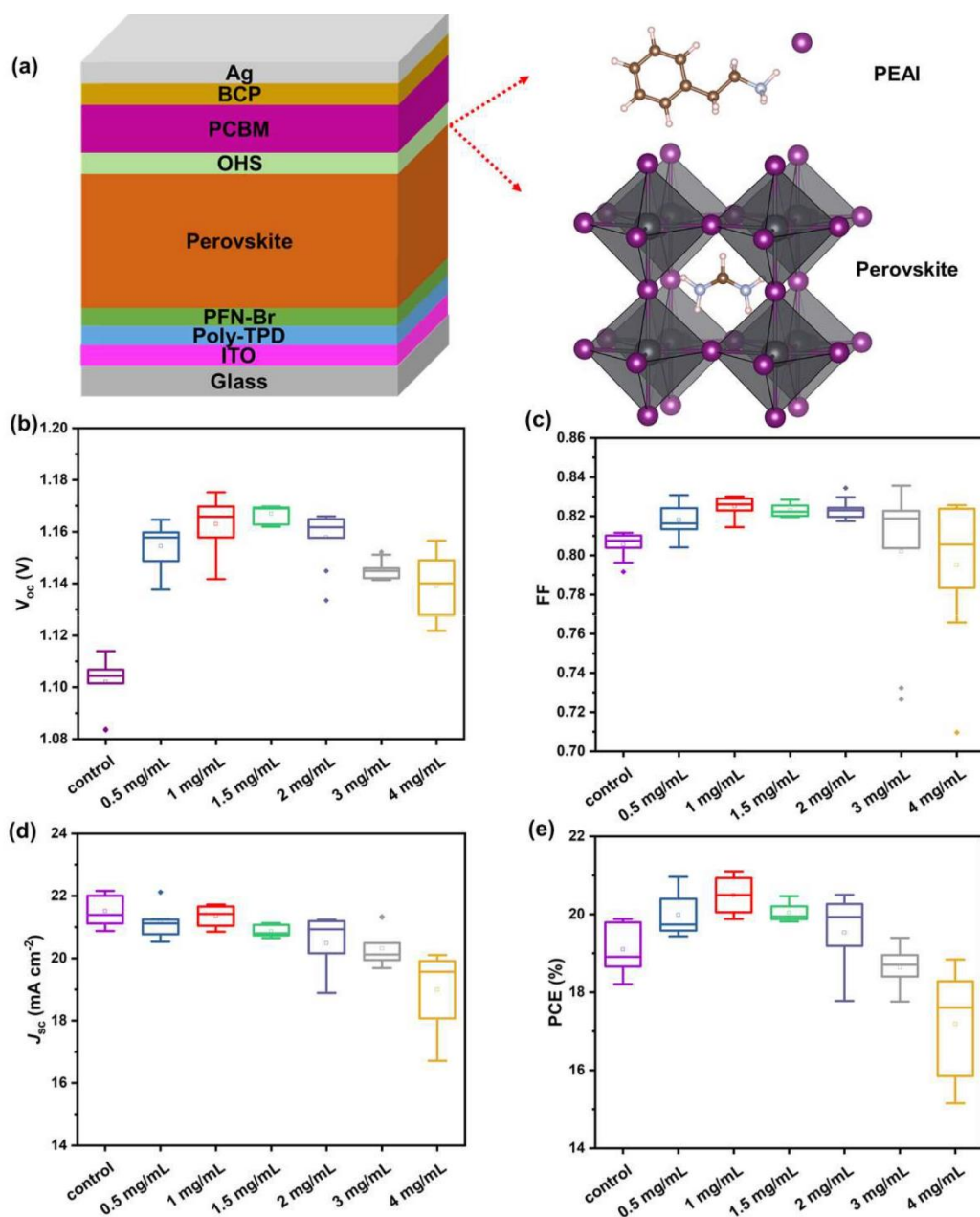
Figure 2. Optimization of OHS treated inverted PSCs. a) Schematic configuration of devices. b-e) Photovoltaic parameters (V_{OC}, J_{SC}, FF and PCE) with the variation of PEAI concentrations. Note that the control is devices without PEAI treatment.

Despite remarkable improvement in the J_{SC}, the devices based on PFN-Br treatment still suffer from a high V_{OC} deficit (defined as $E_g/q - V_{OC}$) of 0.52 V for a 1.64 eV perovskite absorber (see in **Figure S8**). This voltage loss is mainly due to the interfacial recombination at perovskite back contact where fullerene is used as the ETL [31]. As the OHSs on perovskite top interface have shown the potential to further enhance the V_{OC} [39], we first implemented

the FMIE design by directly spin-coating additional phenethylammonium iodide (PEAI) layer on the perovskite surface. After PEAI treatment, the TRPL spectra of perovskite films show a longer PL lifetime (**Figure S9**), implying that PEAI could retard the charge-carrier recombination. We then fabricated devices with the structure shown in **Figure 2a** and further developed the process by optimizing the concentrations of PEAI. As observed in the statistical data from **Figure 2b-e**, PEAI-treated devices exhibit better performance compared to that of control devices within a concentration range from 0.5 to 2 mg mL^{-1} and compromised performance when the PEAI concentration is over 3 mg mL^{-1}. The monotonical decrease of J_{SC} means that PEAI could retard the charge transport due to its insulating nature. The variation of device performance as a function of PEAI concentration indicates that the PEAI layer requires to be cautiously controlled to fulfil its potential. The optimum concentration is found to be 1 mg mL^{-1}, which shows the highest average PCEs. However, when we used the 1 mg mL^{-1} PEAI to treat UV-ozone devices, their performance did not improve as we expected (**Figure S10**). These results demonstrate the synergistic effect of PFN-Br and PEAI treatments in improving the device performance.

By optimizing the process of FMIE, we finally obtained the PSCs with negligible hysteresis in the dark (**Figure 3a**) and under illumination with simulated AM 1.5G solar irradiation at 100 mW cm^{-2} (**Figure 3b**). Remarkably, the champion device shows an increase in V_{OC} to 1.18 V and FF to 0.83, resulting in a PCE of 21.33% (the aperture area is 0.09 cm^2). The integrated current density obtained from EQE spectra is 21.19 mA cm^{-2} (**Figure 3c**), which matches well with the J_{SC} obtained from J-V scans (within 5% error). We tracked the stabilized output of the champion device at the voltage corresponding to the maximum power point (V_{mpp}). As illustrated in **Figure 3d**, the PEAI-treated device (measured outside the glovebox under 1 Sun illumination) shows a stabilized PCE of 21.01 % with an average current density of 21.44 mA cm^{-2}. The long-term stability test was also carried out by tracking the device performance under the lab conditions (without any encapsulation). After 550 h, the device still retained over

70% of its initial PCE (**Figure 3e**).

We also applied other OHSs on the perovskite surface, such as phenylammonium iodide (PAI) and phenylmethylamine iodide (PMAI). All these materials have a similar structure and the main difference comes from the alkyl length in the side chain (**Figure S11**). We fabricated devices based on PAI or PMAI treatments and their corresponding photovoltaic parameters are listed in **Table S3**. Compared to PAI, the PMAI is more favorable for device efficiency by obviously improving the V_{OC}. Different from the previous report in mesoporous structure [40], the PMAI employed in the inverted PSCs did not exhibit any hysteresis in the J-V curves. This once again shows the advantage of the inverted structure. However, although the champion PCE of PMAI reached over 21.5%, the device is unstable at MPP tracking (See in **Figure S12**), indicating the longer alkyl chain of PEAI is beneficial for device stability. Therefore, from the perspective of efficiency and stability, the PEAI is the best choice amongst these OHSs. To demonstrate the impact of PEAI treatment, we further compare the variation of the statistics for the devices without and with PEAI. **Figure 3f** shows the average V_{OC} increasing from 1.10 ± 0.01 to 1.16 ± 0.01 V after PEAI treatment. At the same time, the average FF enhances from 0.79 ± 0.01 to 0.82 ± 0.01 (**Figure 3g**). Notably, the highest FF value is 0.84 ($V_{OC} = 1.16$ V, J_{SC} $= 21.74$ mA cm^{-2}, PCE $= 21.17\%$), which is approaching the fill factor defined by the Shockley–Queisser limit [41,42]. While the average J_{SC} shows a subtle decrease (**Figure 3h**), the average PCE significantly improves from 18.71 ± 0.54 to $20.42 \pm 0.57\%$ (**Figure 3i**).
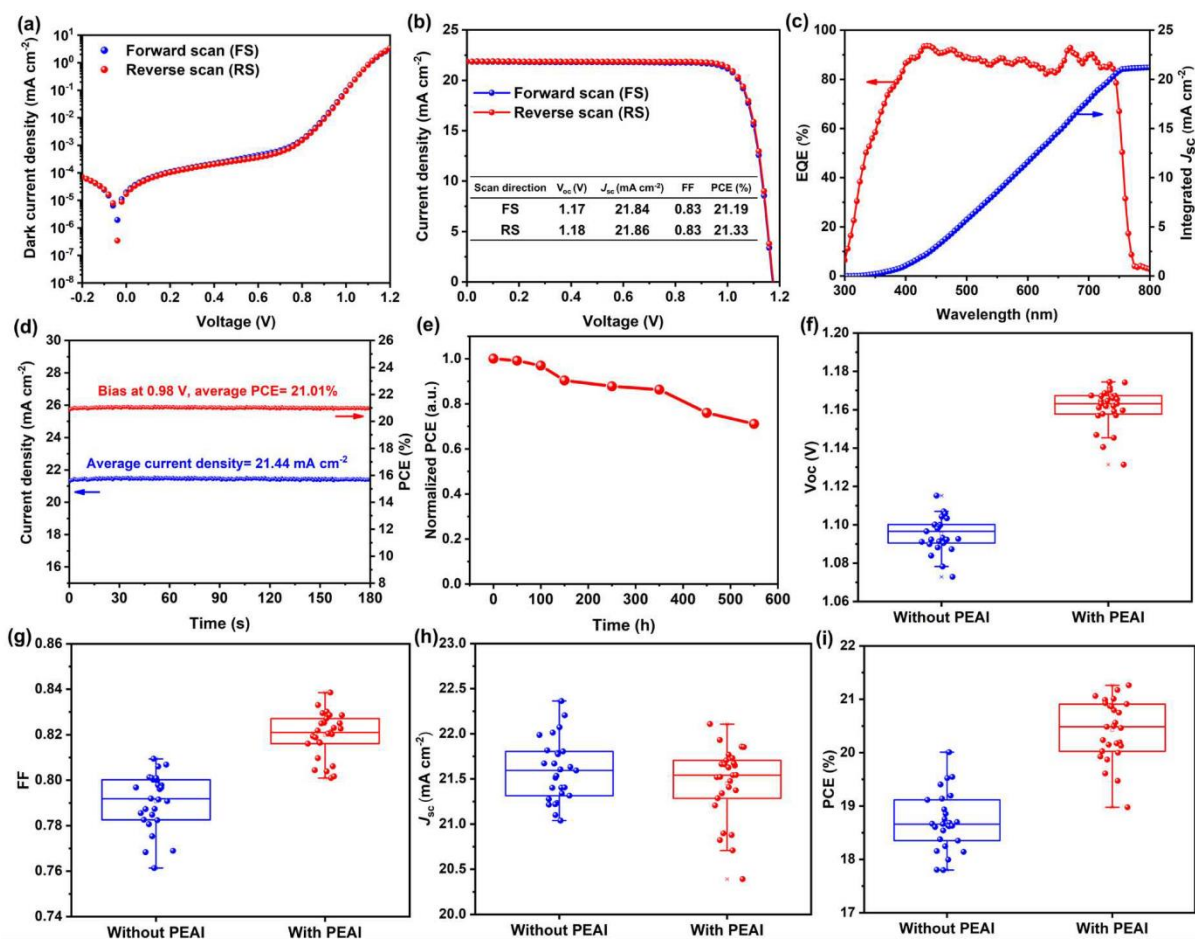
Figure 3. Performances of PEAI treated champion devices. a) Dark J-V curves. b) J-V curves measured under simulated AM 1.5G solar irradiation at 100 mW cm^{-2}. The inset table shows the results obtained from the forward scan (FS, − 0.2 to 1.2 V) and reverse scan (RS, 1.2 to − 0.2 V). c) EQE spectra. d) The stabilized output determined near the maximum power point. e) Shelf-life stability stored in dark at room temperature with relative humidity (RH) of 25-55%. f-i) Statistical distributions of photovoltaic parameters (V_{OC}, FF, J_{SC} and PCE) for devices with or without PEAI treatment. The data are collected based on 27 devices. For each device, the parameters shown here are the average values obtained from the forward and the reverse scans. Note that the devices with the structure of ITO glass/poly-TPD/PFN-Br/perovskite/(with or without PEAI)/PCBM/BCP/Ag.

To understand the origin of device performance enhancement, we performed a range of characterizations of the fabricated devices with or without PEAI treatment. As illustrated in **Figure 4a,b**, both devices show excellent photo-responses under light intensities from 0.1 to 1 Sun, but the PEAI-treated device displays a small fluctuation in the FF under weak light illumination (**Figure S13**). From **Figure 4c**, we note that the PEAI-treated device shows a slope of ~1 for the plot of J_{SC} as a function of light intensity, suggesting reduced non-radiative

14

recombination within the device [43]. Similarly, the light intensity dependence of the V_{OC} is shown in **Figure 4d**. The PEAI-treated device delivers a slope of 1.29 k_BT/q (k_B is the Boltzmann constant, T is temperature, and q is the electric charge), while the control device shows a slope of 1.56 k_BT/q. The lower deviation between the slope and k_BT/q confirms that the defect-assisted (also called Shockley-Read-Hall, SRH) recombination has been further suppressed [39]. Additionally, we conducted the transient photovoltage (TPV) under a white light bias. After PEAI treatment, the TPV decay time shown in **Figure 4e** increases by ~ 3 times than that of the control device, rising from 1.6 to 4.5 μs. The longer TPV decay suggests the slower interfacial charge recombination.
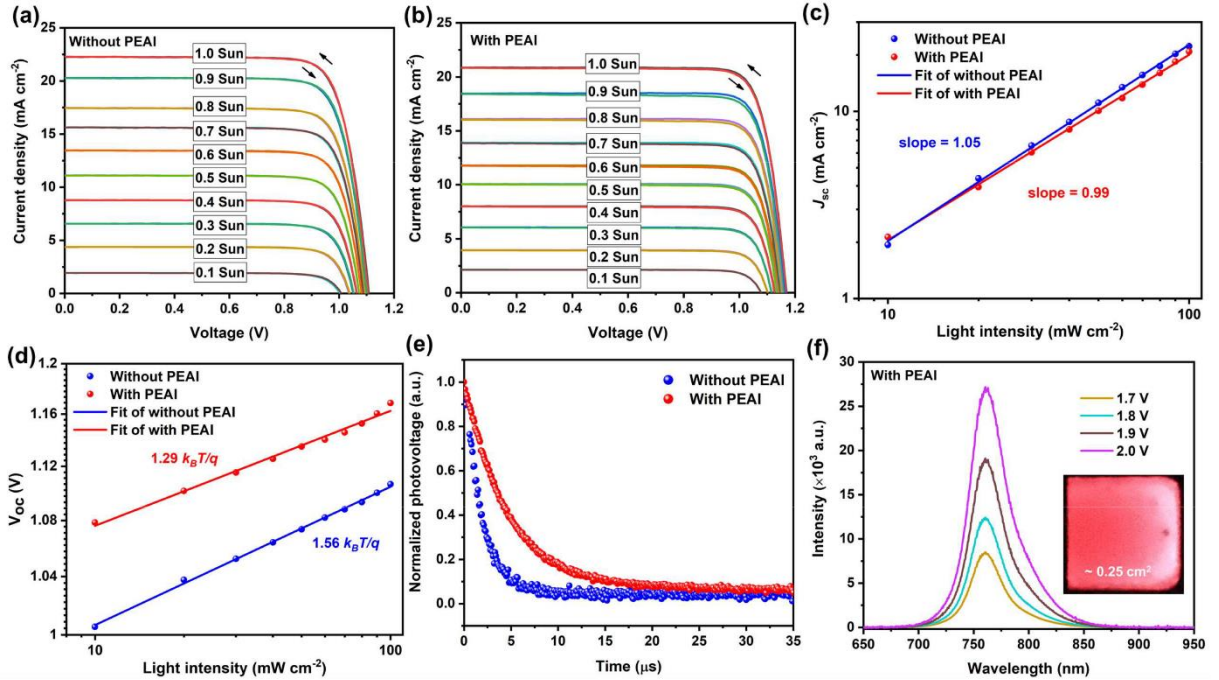
Figure 4. Characterization of devices with or without PEAI treatment. a), b) *J*-V curves measured under light intensities ranging from 0.1 to 1 Sun, consisting of the forward scan (FS, − 0.2 to 1.2 V) and reverse scan (RS, 1.2 to − 0.2 V). c) J_{SC} as a function of light intensities. d) V_{OC} as a function of light intensities. e) Transient photovoltage decay curves. f) EL spectra of a PEAI-treated device. The inset image is the device operating as a LED and showing a bright emission at a bias of 2 V. Note that the devices with the structure of ITO glass/poly-TPD/PFN-Br/perovskite/(with or without PEAI)/PCBM/BCP/Ag.

It is well known that a good solar cell is also a good light-emitting diode (LED). Under the open-circuit condition, the carriers in the absorber could show luminescence while the non-

radiative recombination would impair this process [44]. We measured the electroluminescence (EL) spectra of fabricated PSCs operating as the LEDs to qualitatively assess the non-radiative recombination losses. The PEAI-treated devices show a significantly improved EL intensity compared to those without PEAI treatment (**Figure S14**). And the quantum yield of EL is 1.2% for PEAI-treated device in contrast to the 0.2% for the device without PEAI, suggesting a higher ratio of carriers for the radiative emission. In the meantime, we observe that the EL peak does not shift with the increasing bias as shown in **Figure 4f**. The inset is a photograph of the PEAI-treated device as the LED working at 2 V bias. Hence, these consistent results collectively demonstrate that non-radiative recombination losses present at the contact interface have been considerably mitigated.

To uncover the origin of the reduced recombination losses, we further performed first-principle calculations based on the density functional theory (DFT). In the calculation, the triple-cation perovskite was simplified by the cubic formamidinium lead halide ($FAPbI_3$) to largely reduce the time consumption [23]. To determine the predominant source for defects within the $FAPbI_3$, we estimated the formation energy of all sorts of defects close to surface regions. The formation energy (E_f) is defined by the following equation:

$$E_f = (E_{system} - E_p - E_c)/n \tag{2}$$

where E_{system} is the total energy of the system, E_p is the total energy of charged state perovskite, E_c is the total energy of charged state counterions, and n is the total number of atoms in the slab model. As listed in **Table S4**, the formation energies of I^- and FA^+ vacancies on the surface of the slab model are only -0.0386 and -0.058 eV/atom, respectively. In comparison to other perovskites, such low formation energies indicate these vacancies are capable of co-existing on the surface.
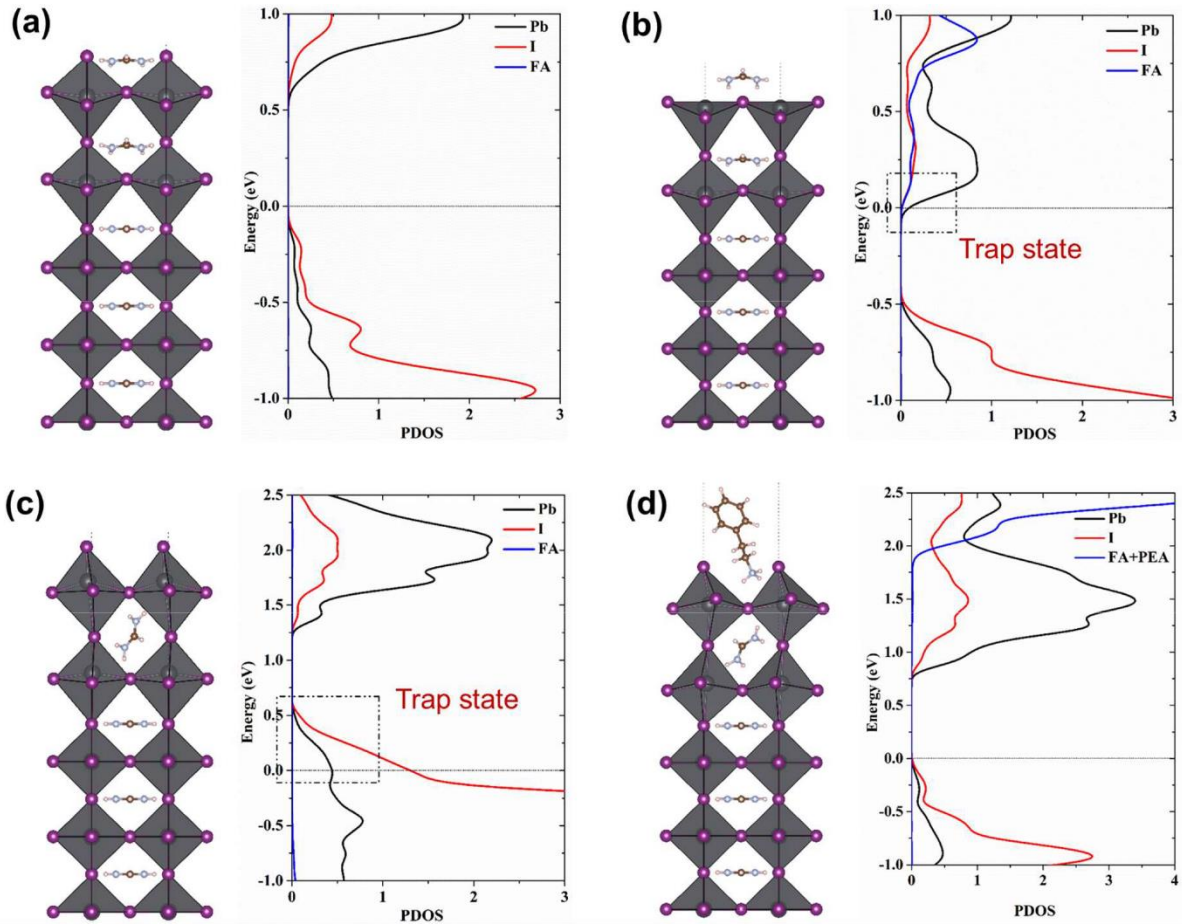
Figure 5. The mechanism of PEAI studied by DFT calculation. a-d) Slab models and corresponding PDOS for different conditions. a) Pristine perovskite. b) Perovskite with I^- vacancies on the surface. c) Perovskite with FA^+ vacancies on the surface. d) Exposed surface passivated by PEAI. Note that the horizontal dotted line indicates the Fermi level.

Figure 5a shows the pristine $FAPbI_3$ (without the PEAI surface treatment) slab model and corresponding projected density of states (PDOS), representing a typical semiconductor with the Fermi level staying in the region of the forbidden band. However, the Fermi level shifts upwards when I^- vacancies emerge on the surface due to the donor doping of I^- (**Figure 5b**). The Fermi level shows a down-shift trend when FA^+ vacancies are created on the surface because of the acceptor state of FA^+ (**Figure 5c**). These impurities might result in the accumulation of charges as trap states being harmful to the transport and collection of electrons or holes. In this work, we spin-coated PEAI solution on the perovskite film directly without additional annealing process, and the PEAI mainly resided at the film surface, as evidenced by

the ToF-SIMS in **Figure S15**. This leads to a question whether or not the PEAI could form a 2D perovskite, like PEA_2PbI_4, or act as a functional molecule on the surface. Here, we cannot observe the 2D characteristics (e.g. platelets) in the SEM image (**Figure S16**) and 2D peaks in the XRD pattern (**Figure S17**) based on PEAI-treated film. These results demonstrate that the spin-coated PEAI cannot form 2D perovskite, consistent with the recent studies [45,39]. Therefore, the functional groups of PEAI are expected to act as the role of surface passivation when coated on top of the perovskite film. The PEAI has the negatively charged iodide ions (I^-) and positively charged phenethylammonium ions (PEA^+). The extra I^- from PEAI tends to occupy the sites of I^- vacancies existing on the exposed surface of $FAPbI_3$ and the PEA^+ species are highly likely to reconcile the FA^+ vacancies. As a result, the perovskite turns to the charge-neutral semiconductor after PEAI treatment as demonstrated in **Figure 5d**. Therefore, DFT calculations confirm that PEAI could passivate the surface defects of perovskite, leading to the mitigated non-radiative recombination at the perovskite/ETL interface that contributes to the enhanced device performance.

4 Conclusion

In summary, we have demonstrated that FMIE is an efficient and facile method that synergistically reduces the interfacial recombination in PSCs in an inverted configuration. Our strategy based on PFN-Br and PEAI treatments in pairs on both contact interfaces of the perovskite film enables us to obtain an inverted PSC with a PCE of 21.33% and a stabilized PCE of 21.01%. Our findings suggest that the simultaneous introduction of functional molecules between perovskite and charge transport layers can further develop high-performance inverted PSCs.

Supporting Information

Supporting Information is available from the website.

Acknowledgments

Author contributions

B. L. and Y. X. contributed equally to this work. B. L. and W. Z. conceived of the work. B. L. fabricated and characterized solar cells. B. L. conducted EQE, SEM, XRD measurements. Z. W. and G. S. conducted the DFT calculations. X. Y., S. A. J. T. and M. T. S. conducted the PL and TRPL measurements. S. H. conducted ToF-SIMS measurements. H. L. conducted AFM measurements. K. D. G. I. J. and I. M. conducted the TPV measurements. T. W. conducted the EL measurements. K. D. G. I. J conducted the EIS measurements. B. L. wrote the first draft of the paper. Y. X., K. D. G. I. J., D. L., S. R. P. S., and W. Z. revised the paper. W. Z. and S. R. P. directed and supervised the project. All authors contributed to the discussion of the results and revision of the manuscript.

Notes

The authors declare no competing financial interest.

References

[1] Q. Wang, Y. Shao, Q. Dong, Z. Xiao, Y. Yuan, J. Huang, Large fill-factor bilayer iodine perovskite solar cells fabricated by a low-temperature solution-process, Energy Environ. Sci. 7 (2014) 2359–2365.

[2] C. Bi, Q. Wang, Y. Shao, Y. Yuan, Z. Xiao, J. Huang, Non-wetting surface-driven high-aspect-ratio crystalline grain growth for efficient hybrid perovskite solar cells, Nat. Commun. 6 (2015) 1–7.

[3] Q. Wang, Q. Dong, T. Li, A. Gruverman, J. Huang, Thin insulating tunneling contacts for efficient and water-resistant perovskite solar cells, Adv. Mater. 28 (2016) 6734–6739.

[4] X. Zheng, B. Chen, J. Dai, Y. Fang, Y. Bai, Y. Lin, H. Wei, X.C. Zeng, J. Huang, Defect passivation in hybrid perovskite solar cells using quaternary ammonium halide anions and cations, Nat. Energy. 2 (2017) 17102.

[5] D. Luo, W. Yang, Z. Wang, A. Sadhanala, Q. Hu, R. Su, R. Shivanna, G.F. Trindade, J.F. Watts, Z. Xu, T. Liu, K. Chen, F. Ye, P. Wu, L. Zhao, J. Wu, Y. Tu, Y. Zhang, X. Yang, W. Zhang, R.H. Friend, Q. Gong, H.J. Snaith, R. Zhu, Enhanced photovoltage for inverted planar heterojunction perovskite solar cells, Science. 360 (2018) 1442–1446.

[6] M. Stolterfoht, C.M. Wolff, J.A. Márquez, S. Zhang, C.J. Hages, D. Rothhardt, S. Albrecht, P.L. Burn, P. Meredith, T. Unold, D. Neher, Visualization and suppression of interfacial recombination for high-efficiency large-area pin perovskite solar cells, Nat. Energy. 3 (2018) 847–854.

[7] X. Liu, Y. Cheng, C. Liu, T. Zhang, N. Zhang, S. Zhang, J. Chen, Q. Xu, J. Ouyang, H. Gong, 20.7% highly reproducible inverted planar perovskite solar cells with enhanced fill factor and eliminated hysteresis, Energy Environ. Sci. 12 (2019) 1622–1633.

[8] S. Bai, P. Da, C. Li, Z. Wang, Z. Yuan, F. Fu, M. Kawecki, X. Liu, N. Sakai, J.T. W. Wang, S. Huettner, S. Buecheler, M. Fahlman, F. Gao, H.J. Snaith, Planar perovskite solar cells with long-term stability using ionic liquid additives, Nature. 571 (2019) 245–250.

[9] S. Tang, Y. Deng, X. Zheng, Y. Bai, Y. Fang, Q. Dong, H. Wei, J. Huang, Composition engineering in doctor-blading of perovskite solar cells, Adv. Energy Mater. 7 (2017) 1700302.

[10] C. Zuo, D. Vak, D. Angmo, L. Ding, M. Gao, One-step roll-to-roll air processed high efficiency perovskite solar cells, Nano Energy. 46 (2018) 185–192.

[11] K.A. Bush, A.F. Palmstrom, Z.J. Yu, M. Boccard, R. Cheacharoen, J.P. Mailoa, D.P. McMeekin, R.L.Z. Hoye, C.D. Bailie, T. Leijtens, I.M. Peters, M.C. Minichetti, N. Rolston, R. Prasanna, S. Sofia, D. Harwood, W. Ma, F. Moghadam, H.J. Snaith, T. Buonassisi, Z.C. Holman, S.F. Bent, M.D. McGehee, 23.6%-efficient monolithic perovskite/silicon tandem solar cells with improved stability, Nat. Energy. 2 (2017) 17009.

[12] L. Mazzarella, Y.H. Lin, S. Kirner, A.B. Morales-Vilches, L. Korte, S. Albrecht, E. Crossland, B. Stannowski, C. Case, H.J. Snaith, R. Schlatmann, Infrared light management using a nanocrystalline silicon oxide interlayer in monolithic perovskite/silicon heterojunction tandem solar cells with efficiency above 25%, Adv. Energy Mater. 9 (2019) 1803241.

[13] Y. Hou, E. Aydin, M. De Bastiani, C. Xiao, F.H. Isikgor, D.J. Xue, B. Chen, H. Chen, B. Bahrami, A.H. Chowdhury, A. Johnston, S.-W. Baek, Z. Huang, M. Wei, Y. Dong, J. Troughton, R. Jalmood, A.J. Mirabelli, T.G. Allen, E. Van Kerschaver, M.I. Saidaminov, D. Baran, Q. Qiao, K. Zhu, S. De Wolf, E.H. Sargent, Efficient tandem solar cells with solution-processed perovskite on textured crystalline silicon, Science. 367 (2020) 1135–1140.

[14] J. Xu, C.C. Boyd, Z.J. Yu, A.F. Palmstrom, D.J. Witter, B.W. Larson, R.M. France, J. Werner, S.P. Harvey, E.J. Wolf, W. Weigand, S. Manzoor, M.F.A.M. van Hest, J.J. Berry, J.M. Luther, Z.C. Holman, M.D. McGehee, Triple-halide wide–band gap perovskites with suppressed phase segregation for efficient tandems, Science. 367 (2020) 1097–1104.

[15] D. Kim, H.J. Jung, I.J. Park, B.W. Larson, S.P. Dunfield, C. Xiao, J. Kim, J. Tong, P. Boonmongkolras, S.G. Ji, F. Zhang, S.R. Pae, M. Kim, S.B. Kang, V. Dravid, J.J. Berry, J.Y. Kim, K. Zhu, D.H. Kim, B. Shin, Efficient, stable silicon tandem cells enabled by anion-engineered wide-bandgap perovskites, Science. (2020) 155–160.

[16] S. Yang, S. Chen, E. Mosconi, Y. Fang, X. Xiao, C. Wang, Y. Zhou, Z. Yu, J. Zhao, Y. Gao, F. De Angelis, J. Huang, Stabilizing halide perovskite surfaces for solar cell operation with wide-bandgap lead oxysalts, Science. 365 (2019) 473–478.

[17] S. Yang, J. Dai, Z. Yu, Y. Shao, Y. Zhou, X. Xiao, X.C. Zeng, J. Huang, Tailoring passivation molecular structures for extremely small open-circuit voltage loss in perovskite solar cells, J. Am. Chem. Soc. 141 (2019) 5781–5787.

[18] M. Zhang, Q. Chen, R. Xue, Y. Zhan, C. Wang, J. Lai, J. Yang, H. Lin, J. Yao, Y. Li, L. Chen, Y. Li, Reconfiguration of interfacial energy band structure for high-performance inverted structure perovskite solar cells, Nat. Commun. 10 (2019) 4593.

[19] H. Choi, C.K. Mai, H.B. Kim, J. Jeong, S. Song, G.C. Bazan, J.Y. Kim, A.J. Heeger, Conjugated polyelectrolyte hole transport layer for inverted-type perovskite solar cells, Nat. Commun. 6 (2015) 7348.

[20] L. Zhang, X. Zhou, X. Zhong, C. Cheng, Y. Tian, B. Xu, Hole-transporting layer based on a conjugated polyelectrolyte with organic cations enables efficient inverted perovskite solar cells, Nano Energy. 57 (2019) 248–255.

[21] Q. Xue, G. Chen, M. Liu, J. Xiao, Z. Chen, Z. Hu, X.F. Jiang, B. Zhang, F. Huang, W. Yang, H.L. Yip, Y. Cao, Improving film formation and photovoltage of highly efficient inverted-type perovskite solar cells through the incorporation of new polymeric hole selective layers, Adv. Energy Mater. 6 (2016) 1502021.

[22] W.Q. Wu, Q. Wang, Y. Fang, Y. Shao, S. Tang, Y. Deng, H. Lu, Y. Liu, T. Li, Z. Yang, A. Gruverman, J. Huang, Molecular doping enabled scalable blading of efficient hole-transport-layer-free perovskite solar cells, Nat. Commun. 9 (2018) 1625.

[23] X. Zheng, Y. Hou, C. Bao, J. Yin, F. Yuan, Z. Huang, K. Song, J. Liu, J. Troughton, N. Gasparini, C. Zhou, Y. Lin, D.J. Xue, B. Chen, A.K. Johnston, N. Wei, M.N. Hedhili, M. Wei, A.Y. Alsalloum, P. Maity, B. Turedi, C. Yang, D. Baran, T.D. Anthopoulos, Y. Han, Z.-H. Lu, O.F. Mohammed, F. Gao, E.H. Sargent, O.M. Bakr, Managing grains and interfaces via ligand anchoring enables 22.3%-efficiency inverted perovskite solar cells, Nat. Energy. 5 (2020) 131–140.

[24] O. Malinkiewicz, A. Yella, Y.H. Lee, G.M. Espallargas, M. Graetzel, M.K. Nazeeruddin,

H.J. Bolink, Perovskite solar cells employing organic charge-transport layers, Nat. Photonics. 8 (2013) 128.

[25] D. Zhao, M. Sexton, H.Y. Park, G. Baure, J.C. Nino, F. So, High-efficiency solution-processed planar perovskite solar cells with a polymer hole transport layer, Adv. Energy Mater. 5 (2014) 1401855.

[26] J.T.W. Wang, Z. Wang, S. Pathak, W. Zhang, D.W. deQuilettes, F. Wisnivesky-Rocca-Rivarola, J. Huang, P.K. Nayak, J.B. Patel, H.A. Mohd Yusof, Y. Vaynzof, R. Zhu, I. Ramirez, J. Zhang, C. Ducati, C. Grovenor, M.B. Johnston, D.S. Ginger, R.J. Nicholas, H.J. Snaith, Efficient perovskite solar cells by metal ion doping, Energy Environ. Sci. 9 (2016) 2892–2901.

[27] X. Xu, C. Ma, Y. Cheng, Y.M. Xie, X. Yi, B. Gautam, S. Chen, H.W. Li, C.S. Lee, F. So, S.W. Tsang, Ultraviolet-ozone surface modification for non-wetting hole transport materials based inverted planar perovskite solar cells with efficiency exceeding 18%, J. Power Sources. 360 (2017) 157–165.

[28] S. Zhang, M. Stolterfoht, A. Armin, Q. Lin, F. Zu, J. Sobus, H. Jin, N. Koch, P. Meredith, P.L. Burn, D. Neher, Interface engineering of solution-processed hybrid organohalide perovskite solar cells, ACS Appl. Mater. Interfaces. 10 (2018) 21681–21687.

[29] J. Lee, H. Kang, G. Kim, H. Back, J. Kim, S. Hong, B. Park, E. Lee, K. Lee, Achieving large-area planar perovskite solar cells by introducing an interfacial compatibilizer, Adv. Mater. 29 (2017) 1606363.

[30] H.K.H. Lee, J. Barbé, S.M.P. Meroni, T. Du, C.T. Lin, A. Pockett, J. Troughton, S.M. Jain, F. De Rossi, J. Baker, M.J. Carnie, M.A. McLachlan, T.M. Watson, J.R. Durrant, W.C. Tsoi, Outstanding indoor performance of perovskite photovoltaic cells–effect of device architectures and interlayers, Sol. RRL. 3 (2019) 1800207.

[31] M. Stolterfoht, P. Caprioglio, C.M. Wolff, J.A. Márquez, J. Nordmann, S. Zhang, D. Rothhardt, U. Hörmann, Y. Amir, A. Redinger, L. Kegelmann, F. Zu, S. Albrecht, N. Koch, T. Kirchartz, M. Saliba, T. Unold, D. Neher, The impact of energy alignment and interfacial recombination on the internal and external open-circuit voltage of perovskite solar cells, Energy Environ. Sci. (2019) 2778–2788.

[32] B. Li, Y. Xiang, K.D.G.I. Jayawardena, D. Luo, J.F. Watts, S. Hinder, H. Li, V. Ferguson, H. Luo, R. Zhu, S.R.P. Silva, W. Zhang, Tailoring perovskite adjacent interfaces by conjugated polyelectrolyte for stable and efficient solar cells, Sol. RRL. (2020) 2000060.

[33] D. Luo, R. Su, W. Zhang, Q. Gong, R. Zhu, Minimizing non-radiative recombination losses in perovskite solar cells, Nat. Rev. Mater. (2019) 44–60.

[34] Z. Wang, M. Deng, X. Xia, Y. Gao, G. Shao, Fundamental basis for distinctive sensing of h_2 in humid environment, Energy Environ. Mater. 1 (2018) 174–178.

[35] H. Xu, Y. Yu, Z. Wang, G. Shao, First principle material genome approach for all solid-state batteries, Energy Environ. Mater. 2 (2019) 234–250.

[36] S. Wu, J. Zhang, Z. Li, D. Liu, M. Qin, S.H. Cheung, X. Lu, D. Lei, S.K. So, Z. Zhu, A.K.Y. Jen, Modulation of defects and interfaces through alkylammonium interlayer for efficient inverted perovskite solar cells, Joule. 4 (2020) 1248–1262.

[37] N. Tripathi, Y. Shirai, M. Yanagida, A. Karen, K. Miyano, Novel surface passivation technique for low-temperature solution-processed perovskite pv cells, ACS Appl. Mater.

Interfaces. 8 (2016) 4644–4650.

[38]   F.X. Xie, D. Zhang, H. Su, X. Ren, K.S. Wong, M. Grätzel, W.C.H. Choy, Vacuum-assisted thermal annealing of $CH_3NH_3PbI_3$ for highly stable and efficient perovskite solar cells, ACS Nano. 9 (2015) 639–646.

[39]   Q. Jiang, Y. Zhao, X. Zhang, X. Yang, Y. Chen, Z. Chu, Q. Ye, X. Li, Z. Yin, J. You, Surface passivation of perovskite film for efficient solar cells, Nat. Photonics. 13 (2019) 460–466.

[40]   H.S. Yoo, N.G. Park, Post-treatment of perovskite film with phenylalkylammonium iodide for hysteresis-less perovskite solar cells, Sol. Energy Mater. Sol. Cells. 179 (2018) 57–65.

[41]   M. Stolterfoht, C.M. Wolff, Y. Amir, A. Paulke, L. Perdigón-Toro, P. Caprioglio, D. Neher, Approaching the fill factor Shockley–Queisser limit in stable, dopant-free triple cation perovskite solar cells, Energy Environ. Sci. 10 (2017) 1530–1539.

[42]   K.D.G.I. Jayawardena, R.M.I. Bandara, M. Monti, E. Butler-Caddle, T. Pichler, H. Shiozawa, Z. Wang, S. Jenatsch, S.J. Hinder, M.G. Masteghin, M. Patel, H.M. Thirimanne, W. Zhang, R.A. Sporea, J. Lloyd-Hughes, S.R.P. Silva, Approaching the Shockley–Queisser limit for fill factors in lead–tin mixed perovskite photovoltaics, J. Mater. Chem. A. 8 (2020) 693–705.

[43]   D. Yang, R. Yang, K. Wang, C. Wu, X. Zhu, J. Feng, X. Ren, G. Fang, S. Priya, S. (Frank) Liu, High efficiency planar-type perovskite solar cells with negligible hysteresis using EDTA-complexed SnO_2, Nat. Commun. 9 (2018) 3239.

[44]   O.D. Miller, E. Yablonovitch, S.R. Kurtz, Strong internal and external luminescence as solar cells approach the shockley–queisser limit, IEEE J. Photovoltaics. 2 (2012) 303–311.

[45]   Y. Wang, T. Zhang, M. Kan, Y. Li, T. Wang, Y. Zhao, Efficient α-$CsPbI_3$ photovoltaics with surface terminated organic cations, Joule. 2 (2018) 2065–2075.